HHS Public Access

Author manuscript

Neurobiol Dis. Author manuscript; available in PMC 2024 January 10.

Published in final edited form as:

Neurobiol Dis. 2023 August ; 184: 106213. doi:10.1016/j.nbd.2023.106213.

Chronic nSMase inhibition suppresses neuronal exosome spreading and sex-specifically attenuates amyloid pathology in APP knock-in Alzheimer's disease mice

Francesca E. Mowry[a], **Francisco Espejo-Porras**[a], **Shijie Jin**[a], **Zainuddin Quadri**[b], **Limin Wu**[c], **Marcela Bertolio**[a], **Rachel Jarvis**[a], **Caroline Reynolds**[a,e], **Rashed Alananzeh**[a], **Erhard Bieberich**[b,d], **Yongjie Yang**[a,e,*]

[a]Department of Neuroscience, Tufts University School of Medicine, 136 Harrison Avenue, Boston, MA 02111, USA

[b]Department of Physiology, University of Kentucky College of Medicine, 780 Rose Street, Lexington, KY 40536, USA

[c]Department of Pediatrics, Massachusetts General Hospital, Harvard Medical School, 55 Fruit Street, Boston, MA 02114, USA

[d]Veterans Affairs Medical Center, 1101 Veterans Drive, Lexington, KY 40502, United States

[e]Graduate School of Biomedical Sciences, Tufts University, 136 Harrison Avenue, Boston, MA 02111, USA

Abstract

Female biased pathology and cognitive decline in Alzheimer's disease (AD) have been consistently observed with unclear underlying mechanisms. Although brain sphingolipid ceramide is elevated in AD patients, whether and how ceramide may contribute to sex-specific differences in amyloid pathology is unknown. Here we investigated the sex-specific impact of chronic pharmacological inhibition of neutral sphingomyelinase (nSMase), a key enzyme responsible for ceramide metabolism, on *in vivo* neuron-derived exosome dynamics, Aβ plaque load, and cognitive function in the $APP^{NL\text{-}F/NL\text{-}F}$ knock-in (APP NL-F) AD mouse model. Our results found sex-specific increase of cortical C20:0 ceramide and brain exosome levels only in APP NL-F but not in age-matched WT mice. Although nSMase inhibition similarly blocks exosome spreading in male and female mice, significantly reduced amyloid pathology was mostly observed in cortex and hippocampus of female APP NL-F mice with only modest effect found on male APP NL-F mice.

*Corresponding author at: Department of Neuroscience, Tufts University School of Medicine, 136 Harrison Ave, Boston, MA 02111, USA. Yongjie.Yang@tudfts.edu (Y. Yang).

Author contributions

FM carried out most of pharmacological administration, Ab42 ELISA, confocal imaging, immunoEM, quantification of amyloid pathology analysis, and behavioral tests. FE performed initial breeding of APP NL-F and $hCD63\text{-}GFP^{f/f}$ breeding and AAV injections. SJ, MB, and LW performed brain exosome isolation and immunoblotting. ZQ and EB performed ceramide HPLC and data analysis. RJ performed behavioral tests and helped maintain mouse colony. RA helped with pharmacological administration and microglial staining and quantification. CR performed AAV injections. FM, RA, ZQ, and YY also performed data analysis. FM also wrote manuscript. YY designed overall study and wrote the manuscript.

Appendix A. Supplementary data

Supplementary data to this article can be found online at https://doi.org/10.1016/j.nbd.2023.106213.

Consistently, T maze test to examine spatial working memory revealed a female-specific reduction in spontaneous alternation rate in APP NL-F mice, which was fully reversed with chronic nSMase inhibition. Together, our results suggest that disease induced changes in ceramide and exosome pathways contribute to the progression of female-specific amyloid pathology in APP NL-F AD models.

Keywords

Alzheimer's disease; nSMase; Ceramide; Exosome; Sex

1. Introduction

Alzheimer's disease (AD), the most common form of dementia, is a progressive brain disease that severely affects memory, reasoning, and behavior and remains one of the most unmet medical challenges. The formation of extracellular β-amyloid plaques from cleaved Aβ peptides and intracellular neurofibrillary tangles (NFTs) composed of hyper-phosphorylated tau protein are considered hallmarks of AD pathology in the brain (Haass et al., 2012; Serrano-Pozo et al., 2011). It has been well observed that these AD pathological features, along with AD prevalence and cognitive decline, are sex dimorphic (Guo et al., 2022; Ferretti et al., 2018). In particular, females have higher AD prevalence rate and are associated with much faster cognitive decline than males with comparable amyloid burden (Buckley et al., 2018). The atrophy rates of hippocampus (and other) brain regions also tend to be faster in female AD patients (Koran et al., 2017). Current mechanistic understanding in female-bias AD prevalence, pathological progression, and cognitive decline remains limited, though the longer life expectancy (Guo et al., 2022) and impact of sex hormone on CNS development and AD pathology (Pike, 2017) have been primarily suggested. Additional factors such as sex chromosomes (Caceres et al., 2020), abnormal Tau accumulation (Deming et al., 2018), and sex-specific neuroinflammation have also been implicated (Guo et al., 2022).

In AD, the amyloid precursor protein (APP) is processed into amyloidogenic Aβ peptide through serial enzymatic steps in subcellular organelles (endosomes/lysosomes and trans-Golgi network) and secreted extracellularly (Haass et al., 2012). Exosomes, the secreted small vesicles that are derived from inward budding of intraluminal vesicles (ILV) inside multiple vesicle bodies (MVBs) (Colombo et al., 2014), have been shown to contribute to the secretion of Aβ peptide and subsequently promote aggregation of Aβ plaques in AD (Malm et al., 2016). Immuno-electron microscopy (EM) staining found that intraneuronal Aβ42 peptides are predominantly localized in MVBs, especially in pyramidal neurons of the cerebral cortex and hippocampus in AD rodent models and human postmortem brains (Takahashi et al., 2002). Exosomal markers are also found near neuritic plaques of AD patient brains (Rajendran et al., 2006). Exosome-mediated secretion of Aβ (Rajendran et al., 2006; Sullivan et al., 2011) and phosphorylated or human mutant tau (Saman et al., 2012; Kanmert et al., 2015) has been found in mouse models and in cerebrospinal fluid (CSF) of AD patients (Street et al., 2012). Microglial exosome-dependent uptake and secretion of mutant tau protein has been shown to play a central role in tauopathy spreading and toxicity

in AD (Asai et al., 2015). However, how exosome signaling contributes to sex-specific AD pathogenesis is essentially unknown.

Although the endosomal sorting complex for transport (ESCRT) is considered the primary cellular machinery involved in ILV biogenesis and exosome secretion (Colombo et al., 2014), a class of sphingolipid ceramides that are hydrolyzed from sphingomyelin by neutral sphingomyelinase (nSMase), have been shown to significantly promote exosome biogenesis and secretion in an ESCRT-independent manner (Trajkovic et al., 2008). Various ceramide species (with different fatty acid chain length) are integral components for cell membrane and play important roles in ROS generation, neuronal apoptosis, and inflammation (Jazvinscak Jembrek et al., 2015). Elevated ceramide levels and nSMase expression in human AD patient brains have been observed (Cutler et al., 2004; Filippov et al., 2012) though whether there is a sex-specific changes remains unexplored. Pharmacological inhibition of nSMase reduces ceramide and exosome levels (Tabatadze et al., 2010; Dinkins et al., 2014) and attenuates Aβ plaques in 5xFAD mice (Dinkins et al., 2014). Similar attenuation of a range of AD pathological features was consistently observed in 5xFAD mice with spontaneous deletion of sphingomyelin phosphodiesterase-3 (Smpd3) gene that encodes nSMase (Dinkins et al., 2016). In the current study, we employed the slow-progressing $APP^{NL\text{-}F/NL\text{-}F}$ knock-in (APP NL-F) AD mouse model (Saito et al., 2014) and cell type-specific exosome reporter CD63-$GFP^{f/f}$ mice (Men et al., 2019) to investigate the sex-specific impact of chronic long-term (from 8 to 13 mo. and 10–18 mo.) nSMase inhibition on *in vivo* neuron-derived exosome dynamics, region-specific Aβ plaque load, and cognitive function.

2. Results

2.1. Female-specific increase of brain exosome quantity in APP NL-F mice

Exosome secretion has been commonly observed in all major CNS cell types in cultures and exosomes are able to be isolated from CNS tissues for detecting disease-specific proteins in various neurodegenerative diseases (Kalani et al., 2014); however, whether exosome quantity varies between males and females especially in AD models remains essentially unexplored. Recent studies have shown that exosomes isolated by ultracentrifugation are often associated with certain secreted proteins (Kim et al., 2022). To better separate proteins from exosomes, we combined size exclusion chromatography that are able to separate based on size with filtration and centrifugation steps (diagram in Fig. 1A) to isolate exosomes from brains of male and female APP NL-F (15-month-old) and age- and sex-matched wild type (WT) control mice. The APP NL-F mice have been shown to not only recapitulate key features but also mimic amyloid pathology in human AD more faithfully than transgenic AD mice (Saito et al., 2014). Nanoparticle tracking analysis (NTA) of isolated exosomes showed a single peak with average size of 140–160 nm across all groups (Fig. 1B), consistent with typical exosome size observed *in vitro*. The mean size and size distribution were shown in Supplemental Fig. S1A. All samples have a mean vesicle size of 220-250 nm and 100-700 nm size distribution. After normalizing exosome quantity by tissue weight (g), we found a significantly higher ($p = 0.04$) brain exosome quantity in female *vs.* male APP NL-F mice (Fig. 1C) but not disease-dependent changes in males and females (Supplemental

Fig. S1B). Interestingly, this sex difference in exosome quantity is not observed in age-matched WT mice, indicating a disease-induced sex difference in exosome quantity in the APP NL-F AD model. To confirm NTA-based exosome quantification, we next performed immunoblotting of Alix (Fig. 1D and Supplemental Fig. S1C), a previously established exosome marker (Colombo et al., 2014), on exosome samples. Consistently, exosomal Alix levels also trended to increase in female APP NL-F ($p = 0.11$, Fig. 1E) but not in WT mice. However, no significant difference in humanized APP expression (only 100 KDa size band detected, Fig. 1F and Supplemental Fig. S1D) and Aβ42 (Fig. 1G) levels were found in brain-derived exosomes of male and female APP NL-F mice. It is unclear whether there is a sex-dimorphic expression of humanized APP in APP NL-F mice. We then examined soluble humanized APP expression from cortical lysates of APP NL-F mice (15-month-old) and found two APP bands (100 and 150 KDa size, respectively) detected by the 6E10 antibody (Supplemental Fig. S1E and F). Subsequent quantification of both APP bands (Supplemental Fig. S1G) found a 30% higher ($p = 0.09$) humanized APP levels in cortex of female than in male APP NL-F mice (15-month-old,). In parallel, we also found significantly higher ($p = 0.04$) humanized soluble Aβ42 levels determined using the specific Aβ42 ELISA in female APP NL-F cortical homogenates (Supplemental Fig. S1H). Overall, these results suggest a female-specific increase in total brain exosomes and consequently exosome-associated APP/Aβ42 cargo in APP NL-F mice.

2.2. In situ association of hCD63-GFP$^+$ neuronal exosomes with 6E10$^+$MET$^+$ and 6E10$^+$MET$^-$ Aβ plaques in cortex of APP NL-F mice

Although exosomal markers such as Alix have been found to colocalize with neuritic plaques in AD brains (Rajendran et al., 2006), immunostaining of exosomal markers (especially surface markers) are ambiguous and non-cell type specific. We have previously generated Cre-dependent exosome reporter hCD63-GFP$^{f/f}$ mice, allowing cell-type specific labeling and tracing of intracellular ILVs and secreted exosomes *in situ* in the brain (Men et al., 2019). With this tool, we have further demonstrated that neuronal exosomes are abundantly present *in vivo* and can spread extensively from the initially secreted site (Men et al., 2019). To examine whether and how humanized APP/Aβ is associated with neuronal exosomes *in situ* in the brain, we performed focal injections of AAV8-CaMKII-mCherry-Cre into the somatosensory cortex of App$^{NL\text{-}F/NL\text{-}F}$hCD63-GFP$^{f/+}$ mice (13-month-old) to selectively label neuronal ILVs and exosomes. As APP is preferentially expressed in neurons and the cleavage of APP into Aβ peptides are primarily occurred in neurons which is then secreted for forming Aβ plaque in AD, we decided to focus on examining the association of humanized APP/Aβ with neuronal exosomes. Abundant hCD63-GFP signals and Aβ aggregates, revealed by 6E10 immunostaining and methoxy-X04 (MET) staining, were found on distal (500 μm) sections from the injection site (Fig. 2A and B). As 6E10 immunostaining labels both soluble and insoluble humanized APP/Aβ but MET selectively labels aggregated fibrillar Aβ structures, 6E10$^+$MET$^-$ plaques are likely to be in the early stage of aggregate formation with mostly soluble humanized APP/Aβ but minimal insoluble Aβ aggregates. The formation of MET$^+$ aggregated fibrillar Aβ had no effect to further deposit exosome signals in aggregates, as hCD63-GFP puncta quantification using Imaris-generated 3D reconstructions from high magnification confocal z-stacks showed that the number of hCD63-GFP$^+$ exosomes are similarly co-localized with both 6E10$^+$MET$^+$

and 6E10^{+}MET^{-} aggregates (Fig. 2C). In addition, we found that hCD63-GFP^{+} exosomes were primarily co-localized with 6E10^{+} immunoreactivity but tend to only surround rather than colocalize with the internal MET^{+} fibrillar Aβ structure (white arrows, Fig. 2A and B), suggesting that exosome structure is unlikely to be inside the insoluble Aβ plaque core. To further examine neuronal exosome localization in relation to Aβ aggregates at higher resolution, we performed immunoEM analysis of GFP on brain sections of AAV-CaMKII-Cre-injected APP$^{NL\text{-}F/NL\text{-}F}$hCD63-GFP$^{f/+}$ mice (23-month-old). Similar to confocal image analysis, hCD63-GFP immunogold signals were also only observed on the peripheral (red box in Fig. 2D, the magnified view in Fig. 2E) but not in the core (yellow box in Fig. 2D, the magnified view in Fig. 2F) of the electron-dense (highlighted in green asterisk, Fig. 2D) Aβ plaque even at the very late stage of disease. Overall, these confocal and immunoEM image analysis supports the notion that it is more likely that neuronal exosomes, by carrying soluble humanized APP/Aβ, facilitate the formation of Aβ aggregates but less likely to spread insoluble Aβ aggregates.

2.3. Disease-induced increase of cortical ceramide levels especially ceramide C20:0 species in female APP NL-F mice

As altered ceramide metabolism has been found in AD brains (Cutler et al., 2004) and ceramide is known to promote exosome biogenesis (Trajkovic et al., 2008), we then determined ceramide levels from the representative somatosensory cortex of male and female APP NL-F mice (15-month-old) and age- and sex-matched WT mice. Ceramide species with different fatty acid length were separated by HPLC, as previously described (Bielawski et al., 2006). The HPLC analysis found that three major ceramide species in cortex, *i.e.*, C18:0, C18:1, and C20:0, with each account for close to or >20% of total ceramide (Fig. 3A). While the relative composition of ceramide species was quite constant across all sex and genotype groups (Fig. 3A), the total ceramide levels in APP NL-F mice were significantly increased ($p = 0.01$) compared to WT mice (Fig. 3B), consistent with previously observed elevation of ceramide levels in AD conditions (Filippov et al., 2012). The increase in total ceramide levels was observed in both male and female APP NL-F mice compared to WT mice, though not statistically different (Supplemental Fig. S2A). Depending on specific ceramide species, there was significant increase of C20:0 observed in both sexes (Supplemental Fig. S2B) and C18:0/C18:1 observed only in male (Supplemental Fig. S2C and D) between WT and APP NL-F mice. However, there is no APP-dependent increase of EVs in males and females (Supplemental Fig. S1B). These results suggest that the disease-dependent increase of C18:0 ceramide may not contribute to exosome-related pathology in APP NL-F mice. On the other hand, while levels of major ceramide species trended higher (though not significantly different, Fig. 3C–E) in WT female compared to WT male mice, modestly but significantly ($p = 0.04$) higher levels of ceramide C20:0 was observed in female APP NL-F mice (Fig. 3E) based on the relative value comparisons. The absolute level-based comparison of major ceramide species between males and females were shown in Supplemental Fig. S2E–G. This is particularly interesting as this higher C20:0 level is in parallel with higher amount of exosomes in APP NL-F females compared to APP NL-F males in Fig. 1C. As C20:0 is also one of the major ceramide species, its significant increase in disease and especially higher level in female APP NL-F mice implicates a potential involvement of C20:0 in female AD exosome-related pathogenesis.

2.4. Chronic inhibition of nSMase suppresses in vivo spreading of neuronal exosomes in both male and female APP NL-F mice

To examine whether ceramide levels sex-specifically affect *in vivo* neuronal exosome spreading and subsequently amyloid pathology, we next pharmacologically inhibited nSMase in APP NL-F mice during early disease stages (Fig. 4A). nSMase is considered the key enzyme involved in the catabolic pathway of ceramide production (Jazvinscak Jembrek et al., 2015), we and others have previously shown that pharmacological inhibition of nSMase by GW4869 significantly reduces ceramide levels and exosome biogenesis (Tabatadze et al., 2010; Dinkins et al., 2014). Whether GW4869 suppresses *in vivo* exosome spreading remains unknown. We administered GW4869 (daily i.p., 1.25 mg/kg) to $APP^{NL\text{-}F/NL\text{-}F}$hCD63-$GFP^{f/+}$ mice from 8mo followed by a single and focal AAV8-CaMKII-mCherry-Cre injection into the somatosensory cortex of mice from 12 m and collected at 13 m so that the hCD63-GFP expression is selectively induced in neurons and the effect of GW4869 on the spreading of hCD63-GFP^+ neuronal exosomes can be monitored. To first confirm that hCD63-GFP^+ neuronal exosomes indeed spread from the injection site but not due to localized induction from AAV8 spreading, we prepared continuous sections (400 μm apart) from the injection site and examined hCD63-GFP and mCherry fluorescence on these sections. Both GFP and mCherry fluorescence signals decreases on sections that are further away from the injection site (Supplemental Fig. S3A); however, clear and abundant CD63-GFP fluorescence was consistently observed on both 600- and 1000 μm sections where mCherry fluorescence has become very restricted or undetectable (Supplemental Fig. S3B), confirming that hCD63-GFP fluorescence at distal sections was not induced by AAV spreading; rather, that these labelled exosomes were secreted and spread from AAV8-CaMKII-mCherry-Cre transduced neurons at the injection site.

To examine how GW4869 administration affects hCD63-GFP distribution and spreading, hCD63-GFP^+ area on serial coronal sections posterior and anterior to the injection site (Fig. 4B and C) were quantified and compared between male and female vehicle- and GW4869-administered groups. We observed a significantly reduced hCD63-GFP^+ area at the injection site (Fig. 4D) but not GFP mean intensity (Fig. 4E), suggesting that AAV injections induce similar hCD63-GFP expression at the injection site but continuous GW4869 administration following the AAV injection reduces exosome biogenesis and spreading even at the injection site. GW4869 administration also significantly and consistently reduced hCD63-GFP^+ area on both posterior and anterior sections (±400 and ± 800 μm) compared to sham groups (except male −800 μm) in both male and female groups (Fig. 4F and G), based on quantification from individually injected mice to eliminate AAV injection variation, demonstrating that blockade of ceramide synthesis is sufficient to suppress *in vivo* neuronal exosome spreading in the cortex.

2.5. Chronic and long-term inhibition of nSMase at early disease and progression stages preferentially attenuates amyloid pathology in female APP NL-F mice

As a slow-progressing AD mouse model, Aβ deposition first appears around 6mo and clear Aβ plaques become evident at 12mo in APP NL-F mice (Saito et al., 2014). However, whether male and female β-amyloid pathology differs in APP NL-F KI mice remains unclear. By performing Methoxy-04 staining, progressive accumulation of Aβ

plaques with age were found in both male and female mice from 8mo to 18mo (Fig. 5A). Interestingly, significantly higher number of Aβ plaques in cortex of female relative to male APP NL-F mice was observed as early as 8mo and persists in 13mo and 18mo (Fig. 5A and B), consistent with human AD pathology that females have more severe amyloid pathology (Babapour Mofrad and van der Flier, 2019). We first determined whether GW4869 administration differentially affected Aβ plaque numbers during early disease period (8mo to 13mo). Long-term and chronic daily administration of GW4869 leads to no obvious gross changes of mice behaviors and significant weight changes (Supplemental Fig. S4A and B). Quantification of MET^+ Aβ plaques in the somatosensory cortex (Fig. 5B and C), entorhinal cortex (Fig. 5D), and hippocampus (Fig. 5E), primary brain regions affected during AD progression, consistently found that GW4869 administration selectively and significantly reduces the number of Aβ plaques in all these regions only in female but not in male APP NL-F mice. In addition, the plaque size in these regions also becomes smaller following GW4869 administration in female mice, indicated by the leftward shift of the size cumulative curve for the larger size plaques (Fig. 5E, the full plaque distribution in corresponding regions in Supplemental Fig. S5 A–C). Meanwhile, it is noted that GW4869 administration only lowers higher female plaque number to male plaque levels without further reduction in these regions (Fig. 5C–E), hinting that nSMase-dependent ceramide synthesis pathway is likely to particularly contribute to more severe amyloid phenotypes in female APP NL-F mice. To determine how ceramide levels correlate with amyloid plaque numbers in sex-dependent manner in APP NL-F mice, we further generated correlation graph between individual major (and total) ceramide species with amyloid plaque numbers (Supplemental Fig. S5 G–J). Interestingly, C20:0 but not other ceramides showed a potential female-biased correlation with amyloid plaque numbers.

Encouraged by these results at early disease phase, we continued to administer GW4869 (daily, i.p) into APP NL-F mice during disease progression from 10mo to 18mo. As shown in Fig. 6A and B, GW4869 drastically reduced overall Aβ plaque numbers especially in the cortex of female mice. Subsequent quantification confirmed that GW4869 significantly reduces MET^+ Aβ plaque number and plaque size in multiple cortical regions in female mice, similarly to early disease phase treatment (Fig. 6C–E). In addition, we found that GW4869 administration also significantly reduces Aβ plaque in both somatosensory and entorhinal cortex of male APP NL-F mice (Fig. 6C and D). The plaque size also trends smaller in these cortical areas (Fig. 6C and D). The full plaque distribution in corresponding regions of 18mo APP NL-F mice is in Supplemental Fig. S5 D–F. As amyloid pathology has progressed significantly more severe in cortex at 18mo age compared to 13mo, the observation that GW4869 administration is able to reduce Aβ plaque numbers in cortex of male APP NL-F mice at 18 (but not 13) months further supports the notion that ceramide is associated with the development of a more severe amyloid pathology. In parallel to this notion, higher Aβ plaque number was observed in the hippocampus of 18mo female mice than in age-matched male mice. Correspondingly, GW4869 administration significantly reduces Aβ plaque number in hippocampus of female APP NL-F mice while has no effect on reducing Aβ plaque number in hippocampus of age-matched male APP NL-F mice.

Microglia have been found to be intimately associated with extracellular Aβ plaques in AD to either attempt clearing these plaques or to constitute a barrier that prevents plaque toxicity

(Bolmont et al., 2008; Condello et al., 2015). Whether nSMase inhibition affects microglia is largely unknown. To examine whether GW4869 affects microglia activity, we then examined GW4869's effect on microglia numbers and association with Aβ plaques in APP NL-F mice. Iba1 immunostaining was performed on cortical sections from APP NL-F mice (Supplemental Fig. S6A). Quantification of $Iba1^+$ microglia number showed an interesting and female-specific increase ($p = 0.01$) in microglia number in the somatosensory cortex of 18-month-old APP NL-F mice following chronic GW4869 administration (Supplemental Fig. S6B). However, the number of microglia associated with plaque is only modestly increased by the GW4869 administration in female APP NL-F mice (Supplemental Fig. S6C). Interestingly, while the number of microglia associated with plaque is linearly increased with plaque size in both male and female mice, there are significantly higher number of microglia associated with plaques (especially larger size) in male than in female mice regardless of the GW4869 administration (Supplemental Fig. S6C), which is on the contrary to observed female-preferential, attenuated effects on amyloid pathology (Fig. 5 and Fig. 6). These results suggest that microglial association with Aβ plaques and their potential phagocytotic clearance are unlikely to mediate GW4869-induced attenuation of amyloid pathology in female APP NL-F mice. Rather, reduced deposition of Aβ, potentially as a result of the inhibition of exosome biogenesis and spreading more likely underlies GW4869's beneficial effects.

To further determine whether GW4869-mediated Aβ plaque reduction in the hippocampus of 18-month-old APP NL-F mice affects cognitive functions, we performed T-maze test from which the spatial working memory is assessed as the average alteration rate (%) across all T maze trials for individual mouse (d'Isa et al., 2021). We found that control WT mice (18mo) typically maintain a 70% alteration rate which is significantly higher than age-matched APP NL-F mice (59%, $p = 0.01$, Fig. 7A), confirming a clear cognitive deficit in APP NL-F mice. Interestingly, this deficit is selectively manifested in female mice (68% in WT; 53% in APP NL-F, p = 0.01, Fig. 7C) but not in male mice (72% in WT; 66% in APP NL-F, $p = 0.32$, Fig. 7B). Excitingly, GW4869 administration completely reversed the alteration rate deficit in APP NL-F mice (p = 0.01, Fig. 7C). In particular, significant rescue was observed in female mice (p = 0.01, Fig. 7C) and a clear but not significant improvement was also found in male mice ($p = 0.18$, Fig. 7B). As T-maze is considered a primarily hippocampus-dependent task, the complete rescue of alternation rate deficit by GW4869 administration in female APP NL-F KI mice is consistent with the selective attenuation of Aβ plaques in female mice.

3. Discussion

Direct evidence to suggest a role of brain lipid in contributing to sex differences in AD pathology remains essentially unknown. As the major carrier for phospholipids and cholesterol in the brain, ApoE polymorphisms (E2, E3, and E4) have been associated with differential risks in AD (Liu et al., 2013). Genetic and epidemiological evidence suggest that females with at least one copy ApoE4 often exhibit faster cognitive decline and deterioration than males (Farrer et al., 1997). Our current study showed that disease induces significant increase in cortical sphingolipid ceramide levels in the APP NL-F AD mouse model. Although sex-specific differences in overall ceramide levels in both WT and

APP NL-F mice are modest, one of the major ceramide species C20:0 is significantly higher in female than in male APP NL-F (but not in WT) mice. In addition, our results found a disease-dependent and significant increase of brain exosome quantity only in female than male APP NL-F but not in WT mice. Although the averaged soluble APP/Aβ42 levels on brain exosomes are not different in female and male APP NL-F mice, the total increased quantity of secreted exosomes, possibly as a result of elevated ceramide C20:0 species, can contribute to a total higher amount of secreted APP/Aβ and subsequently Aβ amyloid load in female APP NL-F mice. Given that the sex difference of the overall ceramide levels in APP NL-F mice is modest, it is also possible that ceramide has a more significant impact on exosome biogenesis pathway in female APP NL-F mice.

Our *in vivo* cell-type specific exosome reporter mice greatly facilitated illustration how the *in vivo* spreading of neuronal exosomes is affected by ceramide synthesis inhibition. Although chronic pharmacological inhibition of the key enzyme nSMase-dependent ceramide synthesis effectively and comparably reduces neuronal exosome spreading in both male and female APP NL-F mice, GW4869 administration selectively attenuates amyloid pathology in female APP NL-F mice at early disease stage and reverses T-maze alteration rate deficits observed in female APP NL-F mice during disease progression. Thus, these results point to a more sensitive response to the inhibition of nSMase-mediated ceramide generation in female APP NL-F mice. Interestingly, female-specific attenuation of amyloid pathology by GW4869 administration only reduces Aβ plaque numbers to baseline (Fig. 5 and Fig. 6) and GW4869 is able to reduce Aβ plaque numbers in cortex of both male and female APP NL-F mice at later disease phase (Fig. 6C and D) when Aβ plaque load becomes more severe. These results suggest that ceramide can be particularly associated with more severe Aβ amyloid pathology in AD conditions that has been consistently observed in females. As cortical ceramide C20:0 has a particular sex difference in APP NL-F mice (Fig. 3E), it is possible that this ceramide species has a unique sex-biased role in amyloid pathology. Note that C20:0 is also increased in both male and female APP NL-F mice compared to WT males and females, respectively, regardless relative (Supplemental S2B) or absolute (Supplemental S2G) value-based comparisons. Because of the long aging and chronic disease progression period in APP NL-F mice, we did not analyze ceramide and brain exosome levels from multiple disease stages in APP NL-F male and female mice which would provide additional important information as to how individual ceramide levels are associated with exosome-related AD pathology development in male and female specific manner. Nevertheless, these results suggest a greater role of ceramide and exosome biogenesis pathway in amyloid pathology of female APP NL-F AD models, providing important new insights to understand sex-specific AD pathogenic mechanisms.

Ceramide has been previously implicated in AD pathogenesis in several pathways (Jazvinscak Jembrek et al., 2015). Increased ceramide levels in pathologically relevant brain regions of AD patients comparing to age-matched controls have been observed (Filippov et al., 2012), which has been associated with oxidative damage in AD. Increased ceramide levels are able to stimulate ROS generation in PC12 cells (Martin et al., 2002) and also facilitates lipid peroxidation (Cutler et al., 2004), which can lead to mitochondria dysfunction and apoptosis. On the other hand, it has been shown that oxidative stress also induces activation of nSMase and results in increased ceramide in H_2O_2-treated PC12 cells

(Martin et al., 2002), becoming a potential negative feedback loop in AD pathogenesis. In addition to oxidative damage, ceramide also forms a pathologically reinforcing cycle with Aβ peptide production. Ceramide promotes β-secretase (BACE1)-mediated cleavage of APP to Aβ peptides by stabilizing membrane localization of BACE1 (Puglielli et al., 2003). Conversely, it has also been shown that soluble and fibrillar Aβ can activate nSMase to further increase ceramide generation (Malaplate-Armand et al., 2006). However, whether there are sex-specific differences in these pathways in AD pathogenesis remains unknown. By specifically analyzing and comparing ceramide levels and exosome quantity and amyloid pathology following GW4869 administration in both male and female mice, our current study provides new insights as to how ceramide may contribute to AD pathogenesis especially in a sex-dependent manner.

Both beneficial and detrimental roles of secreted exosomes in AD pathogenesis have been implicated (Malm et al., 2016). Exosomes can serve as a carrier to either bring Aβ to the site of amyloid formation (Rajendran et al., 2006) thus promoting amyloid pathology or can be internalized into microglia to facilitate Aβ clearance (Yuyama et al., 2014). Prior studies to pharmacologically inhibit and genetically delete nSMase have mostly led to reduced exosome secretion, attenuated Aβ pathology, and improved cognitive function (Dinkins et al., 2014; Dinkins et al., 2016). However, the use of transgenic AD models, such as APP/PS1 and 5XFAD mice, tend to generate much higher Aβ levels that potentially skew the association of Aβ with exosomes and the implication of exosomes in AD pathogenesis. Our current study utilizes the APP NL-F mice to avoid APP overexpression, potentially providing pathologically more relevant evidence in how inhibition of ceramide synthesis affects exosome pathway and amyloid pathology. While the inhibition of nSMase by GW4869 was shown to lead to impaired spatial and episodic-like memory in mice (Tabatadze et al., 2010), we and others consistently showed that GW4869 administration in AD mouse models or genetic nSMase2 deficiency improves cognitive functions (Dinkins et al., 2016). In addition, our results suggest that GW4869-induced attenuation of female amyloid pathology is not mediated by amyloid clearance, as GW4869 only modestly increases microglial association with plaques in female APP NL-F mice, albeit ceramide synthesis inhibition leads to a female-specific increase in microglial numbers. Also, microglial association with plaques is much more significant in male but not in female APP NL-F mice. It is worth to point out that more detailed analysis on microglial phagocytosis of Aβ plaques in male and female APP NL-F mice following GW4869 is needed to further determine the impact of ceramide inhibition of microglial phagocytosis of plaques. In addition, while GW4869 is highly selective to inhibit nSMase activity, it is likely that it may have other inhibitory targets or pathways that contributes to its attenuating effects. Overall, these sex-specific studies provided appealing evidence for the beneficial effect of ceramide synthesis inhibition on attenuating amyloid pathology particularly in slow-progressing female APP NL-F AD mice, thus supporting future nSMase inhibition-based therapeutics especially in female AD patients.

4. Materials and methods

4.1. Animals

App$^{NL\text{-}F/NL\text{-}F}$ knock-in (APP NL-F) mice were obtained from Riken Bioresource Center (Japan). Cre-dependent hCD63-GFP conditional knock-in exosome reporter mice (hCD63-GFP$^{f/f}$) were previously generated and characterized from the lab (Men et al., 2019). APP NL-F mice were crossed with hCD63-GFP$^{f/f}$ mice to generate APP$^{NL\text{-}F/NL\text{-}F}$hCD63-GFP$^{f/+}$ mice. Aged C57BJ/6 wild-type control (WT) mice were obtained from the National Institute on Aging aged rodent colony (NIH). Mice were maintained in temperature- and humidity-controlled rooms on a 12-h light/dark cycle with normal chow and water available *ad libitum*. All experiments were carried out in accordance with the NIH Guide for the Care and Use of Laboratory Animals and the Tufts University Institutional Animal Care and Use Committee guidelines.

4.2. Ceramide analysis

14–15-month-old male and female APP NL-F mice with age- and sex-matched WT controls (n = 4–5 mice/group) were deeply anesthetized with ketamine/xylazine cocktail (100 mg/kg BW ketamine +10 mg/kg BW xylazine in saline; *i.p.*) and transcardially perfused with ice-cold heparinized phosphate-buffered saline (0.1 M, 7.4 pH, PBS; 10 k units heparin/L). Brains were rapidly dissected, snap frozen in 2-methylbutane, and stored at −80 °C until processing. Tissue punches of somatosensory cortex samples were collected in 1.5 mL tubes at −20 °C. After addition of 300 μL Homogenization buffer (0.25 M sucrose, 25 mM KCl, 50 mM Tris CL, and 0.5 mM EDTA), samples were homogenized with WHEATON SAFE-GRIND Potter-ELvehjem Tissue Grinder (CAT#358004) and processed for protein quantification. Ceramide analysis *via* HPLC-MS/MS was performed at the Medical University of South Carolina Lipidomics Shared Resource facility (Charleston, SC), using a Thermo Scientific Vanquish uHPLC system and Thermo Scientific Quantum Access Max triple quadrupole mass spectrometer with an ESI probe set to the multiple reaction monitoring ion mode, as described previously (Bielawski et al., 2010). The raw value obtained for each ceramide species (N-acyl chain lengths = C14:0, C16:0, C18:1, C18:0, C20:0, C22:0, C24:1, C24:0, C26:1, C26:0) was normalized to the tissue homogenate protein concentration (mg/mL) prior to data analysis. Total ceramide species was determined as the sum of all ceramide species measured, with ceramide distribution calculated as relative percent of total ceramide for each species. Absolute lipid levels (pmol/mg) were compared by fold change.

4.3. Exosome isolation and analysis

Brains from 15 to 16-month-old APP NL-F mice and age-matched WT controls (n = 5 mice/group) were used for isolation of brain-derived exosomes. Following ketamine/xylazine overdose (*i.p.*), mice were perfused with ice-cold PBS and brains were rapidly dissected and cut in half along the midline. Half of each brain was processed as individual sample for exosome isolation. After addition of 2 mL enzyme mix (2 mg/mL collagenase D + 40 U/mL Dnase I in Hybernate E solution), tissue was roughly homogenized with a 1 mL pipette tip and incubated for 30 min. at 37 °C, aspirating every 5 min. 20 μL proteinase inhibitor cocktail (P8340, Sigma) was added, and the sample filtered used a 70 μm strainer. After

serial supernatant centrifugation (10 min., 300 *g*, RT; 10 min., 2000 g, 4 °C; 20 min., 5000 g, 4 °C), the final supernatant was passed through a 0.45 μm filter prior to fractionation with qEV 35 Zen2 columns (Izon). Fractions 7 and 8 were collected and concentrated with 30 kDa cut-off tubes (30 min., 4000 g, 4 °C) and resuspended in 200 mL PBS before storing at −80 °C.

4.4. Nanoparticle tracking analysis (NTA)

Exosome samples were resuspended in Dulbecco's phosphate-buffered saline (DPBS) and characterization of EVs was performed by nanoparticle tracking analysis (NTA) using NanoSight LM10 (Malvern Instruments, UK), with screen gain set at 2.0 and camera level at 10.0. Three 60 s measurements were recorded done for each sample. Software NTA 3.2 (Malvern Instruments Ltd., UK) was used for sample-image capturing and data analysis. To calculate the final exosome concentration, the concentration determined by NanoSight software was multiplied by sample dilution and volume, and then normalized to the initial tissue weight (g).

4.5. Immunoblotting

Isolated $APP^{NL\text{-}F}$ and WT exosome samples were lysed with 5× RIPA buffer with Triton X-100 (AAJ62885AD, Fisher) and 25× P8340 (protease inhibitor cocktail) to a final concentration of 1× RIPA +1% P8340. Total protein amount for exosome and cortical homogenate samples was determined using a DC™ Protein Assay Kit II (Bio-Rad) per manufacturer's instructions. For exosome samples, 30 μL of the final lysate was loaded on 4–15% Mini-PROTEAN TGX Stain-Free Protein Gels (Bio-Rad). Tissue homogenates were diluted for a final loading protein content of 30 μg (20 μL loaded per lane). Separated proteins were then transferred onto a PVDF membrane (Bio-Rad) with the Trans-Blot Turbo Transfer System (Bio-Rad). The membrane was blocked with 5% fat-free skim milk in TBST (Tris-buffered saline +0.05% Tween-20) or Super-Block™ T20 (TBS) Blocking Buffer (Thermo Scientific) then incubated with primary antibody overnight at 4 °C (Alix [clone 1A12], 1:500, Santa Cruz; human APP [clone 6E10], 1:1000, BioLegend). Secondary antibodies, including ECL anti-mouse IgG (1:10000, GE Healthcare NA931V) are diluted with Super Blocking Buffer. Bands were visualized on Chemidoc MP imaging system (Bio-Rad) with ECL Plus chemiluminescent substrate (Thermo Fisher Scientific) or Clarity Max Western ECL Substrate (Bio-Rad).

4.6. Human $A\beta_{42}$ ELISA

Soluble human $A\beta_{42}$ was measured in isolated exosome and cortical homogenate samples using the solid-phase sandwich Invitrogen™ Human Aβ42 ELISA Kit (KHB3441), per manufacturer's instructions, and read on an Epoch absorbance microplate reader (BioTek) at 450 nm absorbance with Gen5 3.11 software (BioTek). Interpolated concentrations were normalized to sample protein content prior to data analysis.

4.7. nSMase inhibition

Male and female APP NL-F or $APP^{NL\text{-}F/NL\text{-}F}$hCD63-$GFP^{f/+}$ mice were treated daily (i.p.) with the nSMase inhibitor, GW4869 (GW, 1.25 mg/kg BW/day in DMSO + saline), or

vehicle (VEH, DMSO + saline), from 8- to 13-months (disease onset) or 10- to 18-months-old (disease progression;). GW4869 was obtained from Selleckchem (#S7609). Mice were weighed once per week for dose adjustments (Supplemental Fig. S4). General health-checks were performed on a daily basis in combination with administration. Of the 45 mice treated, two mice were found dead (one VEH APP NL-F female mouse at 17mo age; one GW APP NL-F male mouse at 14mo age), and three mice were humanely euthanized (one VEH APP NL-F male mouse at 14.5mo age, splenomegaly and liver cirrhosis; one VEH APP NL-F female mouse at 13mo.age, rapid weight loss and hepatic pathology; and one GW APP NL-F female mouse at 15mo age, progressive hydrocephalus).

4.8. T maze test

During the final month of intervention, GW and VEH treatment APP NL-F mice underwent behavioral assessment alongside age- and sex-matched WT mice from the NIA aged mouse colony. Additional age- and sex-matched control APP NL-F mice were tested to increase overall group size. WT and APP NL-F control mice were handled on a daily basis for at least 3 weeks prior to testing. Spontaneous alternation behavior in a T maze was used as an assessment of working spatial memory (d'Isa et al., 2021). On three non-consecutive days, each mouse ran four continuous trials after the initial choice run, spending 30 s in the selected arm, with a free return to the start position after each trial (*i.e.*, the opposing arm was closed off after selection and mice were not physically handled between runs). Criteria required that all four limbs be located in an arm for selection to be recorded, and a selection delay ≥60 s was deemed an aborted trial.

4.9. Surgical procedures

AAV8-CaMKII-mCherry-Cre (0.5 μL, 4.00 E + 12 gc/mL) obtained from the University of North Carolina Vector Core was stereotactically injected in the lateral isocortex (−3.0 mm A/P, 3.5 mm M/L, −0.9 mm D/V) of a cohort of $APP^{NL\text{-}F/NL\text{-}F}$hCD63-$GFP^{f/+}$ mice from the 8–13-month group one weeks prior to the end of treatment. Surgeries were performed under isoflurane anesthesia with perioperative administration of buprenorphine SR-LAB (s.q.; 2 mL/kg BW). Briefly, mice were fixed in a stereotaxic frame and injection sites determined relative to bregma. Burr holes were made using a handheld drill and coordinates rechecked prior to injection with a Hamilton syringe attached to an automatic injector at a rate of 100 nL/min. Post-operative checks were conducted for three days, with re-administration of buprenorphine SR-LAB every 48–72 h, as needed.

4.10. Immunohistochemistry

Mice were anesthetized under isoflurane and subsequently administered an overdose of ketamine/xylazine cocktail. After respiratory arrest, mice were transcardially perfused with ice-cold heparinized PBS followed by 4% PFA. Brains were dissected, post-fixed overnight in 4% PFA at 4 °C, cryoprotected in 30% sucrose, and stored at −80 ° *C. prior* to sectioning, brains were embedded in OCT-Compound Tissu-Tek (Sakura; Tokyo, Japan). Serial 20-μm-thick coronal sections containing the somatosensory cortex, hippocampus, and entorhinal cortex were collected at −20 °C using a Leica HM525 cryostat and mounted directly onto SuperFrost Plus slides (Fisher Scientific). Sections were air-dried and stored at −80 °C prior to processing. Prior to sacrifice, mice received an *i.p.* injection of methoxy-X04 (MET, 10

mg/kg BW in 5% DMSO + saline), a fluorescent derivative of Congo red and Chrysamine-G that readily crosses the blood-brain barrier and binds Aβ fibrils *in vivo* (Klunk et al., 2002). MET was obtained from Tocris (#4920). Alternatively, to stain mounted sections directly, slides were washed 3 × 5 min. in PBS, incubated for 3 h at RT in 10 μM MET + PBS, rinsed for 30 s in 40% ethanol + PBS, and rinsed for 30 s in 80% ethanol + PBS. For microglia and humanized APP labeling, mounted slides were washed 3 × 5 min. in PBS and blocked for 1 h in 10% goat serum +0.3% PBS + Triton X-100 (PBST). Blocking solution was replaced with primary antibodies: rabbit anti-Iba1 antibody (1:1000, FUJIFILM Wako Pure Chemical Corporation, #19–019741) or APP antibody (clone 6E10, 1:250, Novus Biologicals, NBP2–62566) in 5% goat serum +0.3% PBST, and left to incubate overnight at RT. After 3 × 5 min. Washes in PBS, secondary antibody cocktail was added (1:250 goat anti-rabbit Alexa555 IgG [Invitrogen, CAT#A21428] + 5% goat serum in 0.3% PBST) for 90 min. Slides were washed 3 × 5 min. in PBS and coverslipped with Prolong TM Gold antifade mounting media.

4.11. Image acquisition and analysis

Confocal z-stack imaging of neuron-derived hCD63-GFP association with 6E10- and MET-labelled plaques was performed on a Nikon A1R confocal laser scanning microscope using a 60× objective with oil. Stacks were imported to Imaris to generate 3D reconstructions of GFP and 6E10 channels for calculation of GFP puncta/plaque. The number of puncta was normalized to plaque volume and compared between 6E10 + MET+ and 6E10 + MET− plaques. For quantification of neuron-derived hCD63-GFP signal spreading, single-plane low magnification images were taken on a Zeiss Axio Imager with a 2.5× objective lens, and densitometry analyses performed in ImageJ. Briefly, an ROI was manually drawn prior to thresholding and measurement of GFP^+ signal area and mean fluorescence intensity. Signal decay for sections from individual mice was calculated as the percent GFP^+ signal area at a given distance relative to the area of IF signal at the injection site (set as 100%). To assess Aβ plaque load, 10× magnification single-plane images of MET-stained plaques within each region were acquired on a Zeiss Axio Imager and imported to ImageJ for analysis with the Analyze Particles plugin. Plaque burden was characterized by the average number of plaques within a given region (*i.e.*, somatosensory cortex, hippocampus, or entorhinal cortex) per image for each mouse, alongside cumulative relative frequency distribution curves of individual plaque sizes for each group. For microglial analyses, 20× magnification full-thickness z-stacks of IBA1- and MET-stained sections were acquired on a Nikon A1R confocal laser scanning microscope. Microglia counts were performed using the Cell Counter plugin for ImageJ from maximum projection images of IBA1 staining, with plaque-associated microglia determined as $IBA1^+$ cells within a 20 μm radius of MET-stained plaques.

4.12. Immuno-electron microcopy

Mice were deeply anesthetized and transcardially perfused with ice-cold heparinized PBS followed by fixation with 4% PFA + 0.25% glutaraldehyde in PBS. Brains were dissected, post-fixed overnight at 4 °C, and transferred to PBS. 100 μm coronal sections were cut on a vibratome, collected in PBS, and processed for 5 nm immunogold labeling of GFP at

the Harvard Medical School Electron Microscopy Core facility. Images were acquired on a JEOL 1200EX transmission electron microscope.

4.13. Statistics

Data sets were analyzed using GraphPad Prism 9 software (La Jolla, CA, USA) and presented as mean ± SEM. Data sets were compared using two-tailed Student's *t*-tests or one- and two-way ANOVA with post-hoc Tukey testing, as indicated in figure legends. Comparison of fit non-linear regression analyses were used to compare plaque size cumulative frequency distribution curves. Statistical significance was set at $\alpha = 0.05$.

Supplementary Material

Refer to Web version on PubMed Central for supplementary material.

Acknowledgments

This work was supported by NIH grants AG059610, AG078728, and NS125490 (YY). Imaging and genomic work was performed with the assistance of the Tufts Center for Neuroscience Research. EM was performed with the assistance of the Harvard Medical School EM Core Facility. Ceramide analysis was carried at the Medical University of South Carolina Lipidomics Shared Resource facility (Charleston, SC).

Data availability

All data sets supporting this current study are available upon request to the corresponding author.

Abbreviations

AD	Alzheimer's disease
APP	amyloid precursor protein
APP NL-F	$APP^{NL-F/NL-F}$ knock-in
CSF	cerebrospinal fluid
ESCRT	endosomal sorting complex for transport
ILV	intraluminal vesicle
MET	methoxy-X04
MVB	multivesicular body
nSMase	neutral sphingomyelinase
NFT	neurofibrillary tangle
NTA	nanoparticle tracking analysis
Smpd3	sphingomyelin phosphodiesterase-3
WT	wild-type

References

Asai H, Ikezu S, Tsunoda S, Medalla M, Luebke J, Haydar T, et al. , 2015. Depletion of microglia and inhibition of exosome synthesis halt tau propagation. Nat. Neurosci 18 (11), 1584–1593. [PubMed: 26436904]

Babapour Mofrad R, van der Flier WM, 2019. Nature and implications of sex differences in AD pathology. Nat. Rev. Neurol 15 (1), 6–8. [PubMed: 30542072]

Bielawski J, Szulc ZM, Hannun YA, Bielawska A, 2006. Simultaneous quantitative analysis of bioactive sphingolipids by high-performance liquid chromatography-tandem mass spectrometry. Methods. 39 (2), 82–91. [PubMed: 16828308]

Bielawski J, Pierce JS, Snider J, Rembiesa B, Szulc ZM, Bielawska A, 2010. Sphingolipid analysis by high performance liquid chromatography-tandem mass spectrometry (HPLC-MS/MS). Adv. Exp. Med. Biol 688, 46–59. [PubMed: 20919645]

Bolmont T, Haiss F, Eicke D, Radde R, Mathis CA, Klunk WE, et al. , 2008. Dynamics of the microglial/amyloid interaction indicate a role in plaque maintenance. J. Neurosci 28 (16), 4283–4292. [PubMed: 18417708]

Buckley RF, Mormino EC, Amariglio RE, Properzi MJ, Rabin JS, Lim YY, et al. , 2018. Sex, amyloid, and APOE epsilon4 and risk of cognitive decline in preclinical Alzheimer's disease: findings from three well-characterized cohorts. Alzheimers Dement. 14 (9), 1193–1203. [PubMed: 29803541]

Caceres A, Jene A, Esko T, Perez-Jurado LA, Gonzalez JR, 2020. Extreme downregulation of chromosome Y and Alzheimer's disease in men. Neurobiol. Aging 90 (150), e1–e4.

Colombo M, Raposo G, Thery C, 2014. Biogenesis, secretion, and intercellular interactions of exosomes and other extracellular vesicles. Annu. Rev. Cell Dev. Biol 30, 255–289. [PubMed: 25288114]

Condello C, Yuan P, Schain A, Grutzendler J, 2015. Microglia constitute a barrier that prevents neurotoxic protofibrillar Abeta42 hotspots around plaques. Nat. Commun 6, 6176. [PubMed: 25630253]

Cutler RG, Kelly J, Storie K, Pedersen WA, Tammara A, Hatanpaa K, et al. , 2004. Involvement of oxidative stress-induced abnormalities in ceramide and cholesterol metabolism in brain aging and Alzheimer's disease. Proc. Natl. Acad. Sci. U. S. A 101 (7), 2070–2075. [PubMed: 14970312]

Deming Y, Dumitrescu L, Barnes LL, Thambisetty M, Kunkle B, Gifford KA, et al. , 2018. Sex-specific genetic predictors of Alzheimer's disease biomarkers. Acta Neuropathol. 136 (6), 857–872. [PubMed: 29967939]

Dinkins MB, Dasgupta S, Wang G, Zhu G, Bieberich E, 2014. Exosome reduction in vivo is associated with lower amyloid plaque load in the 5XFAD mouse model of Alzheimer's disease. Neurobiol. Aging 35 (8), 1792–1800. [PubMed: 24650793]

Dinkins MB, Enasko J, Hernandez C, Wang G, Kong J, Helwa I, et al. , 2016. Neutral Sphingomyelinase-2 deficiency ameliorates Alzheimer's disease pathology and improves cognition in the 5XFAD mouse. J. Neurosci 36 (33), 8653–8667. [PubMed: 27535912]

d'Isa R, Comi G, Leocani L, 2021. Apparatus design and behavioural testing protocol for the evaluation of spatial working memory in mice through the spontaneous alternation T-maze. Sci. Rep 11 (1), 21177. [PubMed: 34707108]

Farrer LA, Cupples LA, Haines JL, Hyman B, Kukull WA, Mayeux R, et al. , 1997. Effects of age, sex, and ethnicity on the association between apolipoprotein E genotype and Alzheimer disease. A meta-analysis. APOE and Alzheimer disease Meta analysis consortium. JAMA. 278 (16), 1349–1356. [PubMed: 9343467]

Ferretti MT, Iulita MF, Cavedo E, Chiesa PA, Schumacher Dimech A, Santuccione Chadha A, et al. , 2018. Sex differences in Alzheimer disease - the gateway to precision medicine. Nat. Rev. Neurol 14 (8), 457–469. [PubMed: 29985474]

Filippov V, Song MA, Zhang K, Vinters HV, Tung S, Kirsch WM, et al. , 2012. Increased ceramide in brains with Alzheimer's and other neurodegenerative diseases. J. Alzheim. Disease : JAD 29 (3), 537–547.

Guo L, Zhong MB, Zhang L, Zhang B, Cai D, 2022. Sex differences in Alzheimer's disease: insights from the multiomics landscape. Biol. Psychiatry 91 (1), 61–71. [PubMed: 33896621]

Haass C, Kaether C, Thinakaran G, Sisodia S, 2012. Trafficking and proteolytic processing of APP. Cold Spring Harb. Perspect. Med 2 (5), a006270. [PubMed: 22553493]

Jazvinscak Jembrek M, Hof PR, Simic G, 2015. Ceramides in Alzheimer's disease: key mediators of neuronal apoptosis induced by oxidative stress and Abeta accumulation. Oxidative Med. Cell. Longev 2015, 346783.

Kalani A, Tyagi A, Tyagi N, 2014. Exosomes: mediators of neurodegeneration, neuroprotection and therapeutics. Mol. Neurobiol 49 (1), 590–600. [PubMed: 23999871]

Kanmert D, Cantlon A, Muratore CR, Jin M, O'Malley TT, Lee G, et al. , 2015. C-terminally truncated forms of tau, but not full-length tau or its C-terminal fragments, are released from neurons independently of cell death. J. Neurosci 35 (30), 10851–10865. [PubMed: 26224867]

Kim G, Chen X, Yang Y, 2022. Pathogenic extracellular vesicle (EV) signaling in amyotrophic lateral sclerosis (ALS). Neurotherapeutics. 19 (4), 1119–1132. [PubMed: 35426061]

Klunk WE, Bacskai BJ, Mathis CA, Kajdasz ST, McLellan ME, Frosch MP, et al. , 2002. Imaging Abeta plaques in living transgenic mice with multiphoton microscopy and methoxy-X04, a systemically administered Congo red derivative. J. Neuropathol. Exp. Neurol 61 (9), 797–805. [PubMed: 12230326]

Koran MEI, Wagener M, Hohman TJ, Alzheimer's, Neuroimaging I., 2017. Sex differences in the association between AD biomarkers and cognitive decline. Brain Imag. Behav 11 (1), 205–213.

Liu CC, Liu CC, Kanekiyo T, Xu H, Bu G, 2013. Apolipoprotein E and Alzheimer disease: risk, mechanisms and therapy. Nat. Rev. Neurol 9 (2), 106–118. [PubMed: 23296339]

Malaplate-Armand C, Florent-Bechard S, Youssef I, Koziel V, Sponne I, Kriem B, et al. , 2006. Soluble oligomers of amyloid-beta peptide induce neuronal apoptosis by activating a cPLA2-dependent sphingomyelinase-ceramide pathway. Neurobiol. Dis 23 (1), 178–189. [PubMed: 16626961]

Malm T, Loppi S, Kanninen KM, 2016. Exosomes in Alzheimer's disease. Neurochem. Int 97, 193–199. [PubMed: 27131734]

Martin D, Salinas M, Fujita N, Tsuruo T, Cuadrado A, 2002. Ceramide and reactive oxygen species generated by H2O2 induce caspase-3-independent degradation of Akt/protein kinase B. J. Biol. Chem 277 (45), 42943–42952. [PubMed: 12213802]

Men Y, Yelick J, Jin S, Tian Y, Chiang MSR, Higashimori H, et al. , 2019. Exosome reporter mice reveal the involvement of exosomes in mediating neuron to astroglia communication in the CNS. Nat. Commun 10 (1), 4136. [PubMed: 31515491]

Pike CJ, 2017. Sex and the development of Alzheimer's disease. J. Neurosci. Res 95 (1–2), 671–680. [PubMed: 27870425]

Puglielli L, Ellis BC, Saunders AJ, Kovacs DM, 2003. Ceramide stabilizes beta-site amyloid precursor protein-cleaving enzyme 1 and promotes amyloid beta-peptide biogenesis. J. Biol. Chem 278 (22), 19777–19783. [PubMed: 12649271]

Rajendran L, Honsho M, Zahn TR, Keller P, Geiger KD, Verkade P, et al. , 2006. Alzheimer's disease beta-amyloid peptides are released in association with exosomes. Proc. Natl. Acad. Sci. U. S. A 103 (30), 11172–11177. [PubMed: 16837572]

Saito T, Matsuba Y, Mihira N, Takano J, Nilsson P, Itohara S, et al. , 2014. Single app knock-in mouse models of Alzheimer's disease. Nat. Neurosci 17 (5), 661–663. [PubMed: 24728269]

Saman S, Kim W, Raya M, Visnick Y, Miro S, Jackson B, et al. , 2012. Exosome-associated tau is secreted in tauopathy models and is selectively phosphorylated in cerebrospinal fluid in early Alzheimer disease. J. Biol. Chem 287 (6), 3842–3849. [PubMed: 22057275]

Serrano-Pozo A, Frosch MP, Masliah E, Hyman BT, 2011. Neuropathological alterations in Alzheimer disease. Cold Spring Harb. Perspect. Med 1 (1), a006189. [PubMed: 22229116]

Street JM, Barran PE, Mackay CL, Weidt S, Balmforth C, Walsh TS, et al. , 2012. Identification and proteomic profiling of exosomes in human cerebrospinal fluid. J. Transl. Med 10, 5. [PubMed: 22221959]

Sullivan CP, Jay AG, Stack EC, Pakaluk M, Wadlinger E, Fine RE, et al. , 2011. Retromer disruption promotes amyloidogenic APP processing. Neurobiol. Dis 43 (2), 338–345. [PubMed: 21515373]

Tabatadze N, Savonenko A, Song H, Bandaru VV, Chu M, Haughey NJ, 2010. Inhibition of neutral sphingomyelinase-2 perturbs brain sphingolipid balance and spatial memory in mice. J. Neurosci. Res 88 (13), 2940–2951. [PubMed: 20629193]

Takahashi RH, Milner TA, Li F, Nam EE, Edgar MA, Yamaguchi H, et al. , 2002. Intraneuronal Alzheimer abeta42 accumulates in multivesicular bodies and is associated with synaptic pathology. Am. J. Pathol 161 (5), 1869–1879. [PubMed: 12414533]

Trajkovic K, Hsu C, Chiantia S, Rajendran L, Wenzel D, Wieland F, et al. , 2008. Ceramide triggers budding of exosome vesicles into multivesicular endosomes. Science. 319 (5867), 1244–1247. [PubMed: 18309083]

Yuyama K, Sun H, Sakai S, Mitsutake S, Okada M, Tahara H, et al. , 2014. Decreased amyloid-beta pathologies by intracerebral loading of glycosphingolipid-enriched exosomes in Alzheimer model mice. J. Biol. Chem 289 (35), 24488–24498. [PubMed: 25037226]

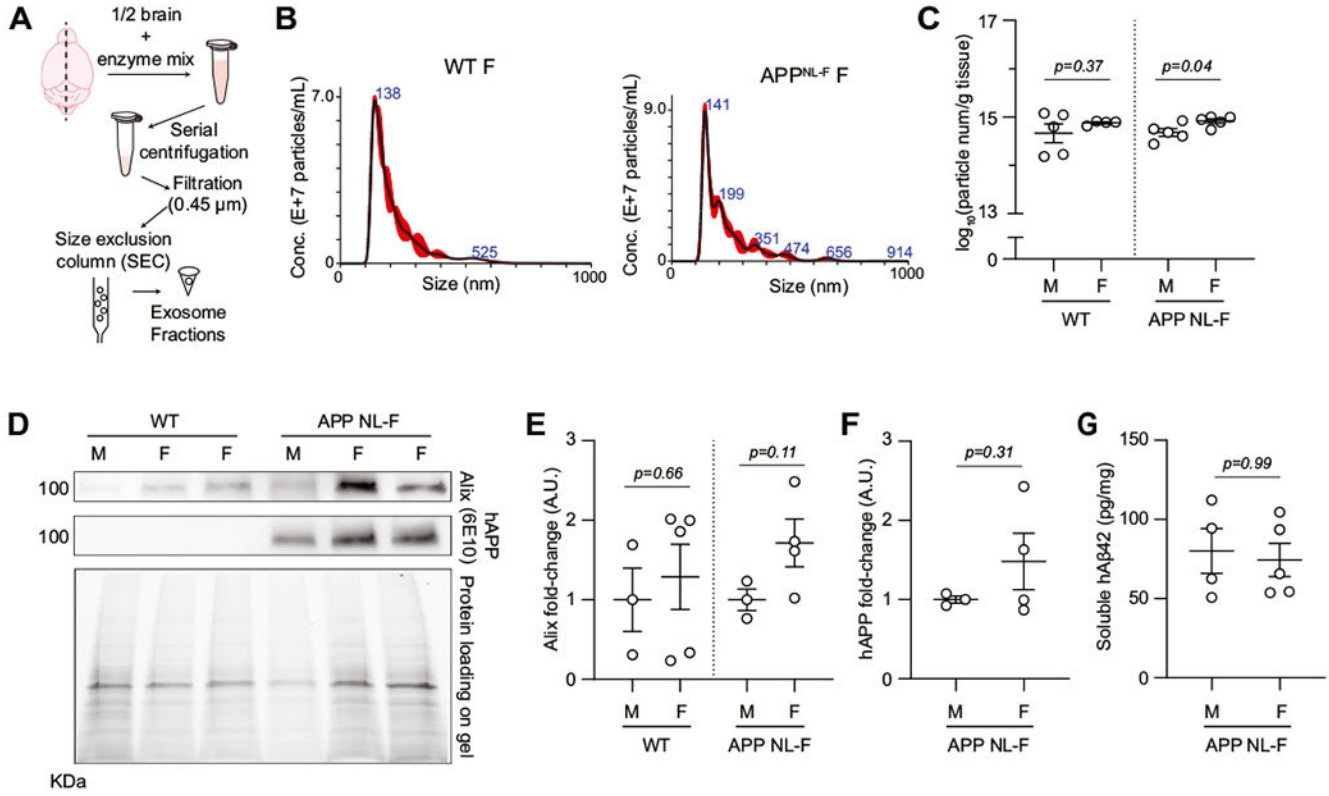

Fig. 1.

Female-specific increase of brain exosome quantity in APP NL-F mice.

(A) Schematic diagram of exosome isolation procedures from fresh brain tissues. (B) Representative particle size distribution trace of diluted exosome samples from WT and APP NL-F mice from nanoparticle tracking analysis (NTA). (C) Total exosome concentration for each half-brain sample, as determined by NTA, in 15–16-month-old male and female WT and APP NL-F mice. Values were calculated based on dilution factor, normalized to half-brain weight (g), and converted as $\log_{10}$(particles/g tissue); n = 4–5 mice/group. (D) Representative immunoblots for Alix (exosome marker) and humanized APP (detected by the 6E10 clone) in brain-derived exosome samples. Note that the full view of immunoblots in Supplemental Fig. S1C and D (immunoblot 1). Quantification of Alix (E) and humanized APP (F) in brain-derived exosome samples. Specific band volume immunoreactivity was normalized to total protein content (mg) and displayed as fold-change relative to respective males; n = 3–5 mice/group. (G) Soluble human $A\beta_{42}$ detected by ELISA in isolated exosome samples from APP NL-F mice ($hA\beta_{42}$ normalized to protein concentration); n = 4–5 mice/group. P values determined by Student's t-test and data shown as mean ± SEM.

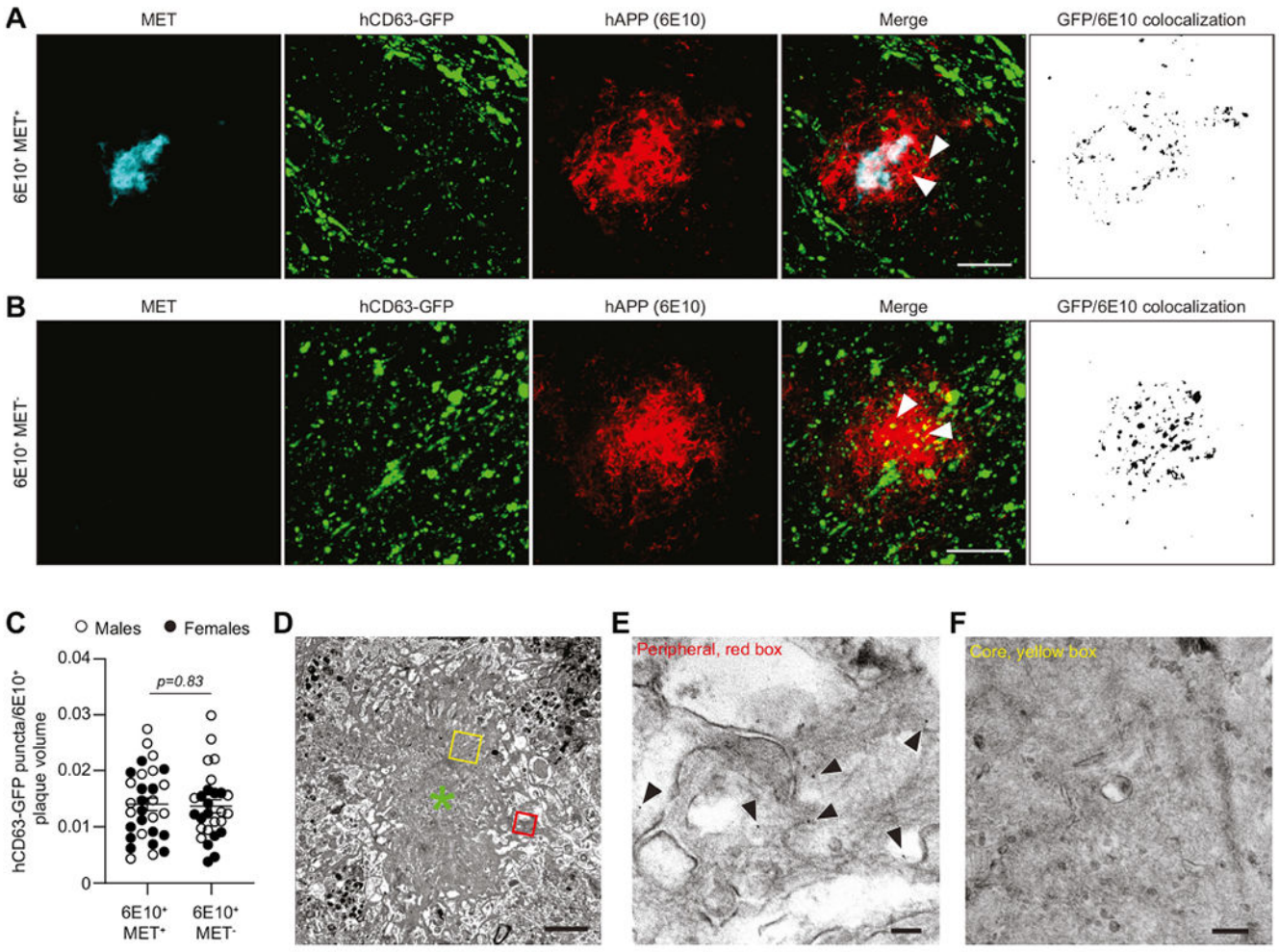

Fig. 2.

In situ association of neuronal hCD63-GFP with 6E10^{+}MET^{+} and 6E10^{+}MET^{-} plaques. Representative maximum projection images from confocal z-stacks of 6E10^{+}MET^{+} (**A**) and $^{+}$MET^{-} (**B**) plaques in the lateral side of cortex of a 13-month-old App$^{NL\text{-}F/NL\text{-}F}$CD63$^{f/+}$ female after a focal injection of AAV8-CaMKII-mCherry-Cre to induce neuron-specific hCD63-GFP expression (green). Sections were stained with methoxy-X04 (MET; blue) and 6E10 (red) and imaged with a 60×-mag. Objective (scale bars = 20 μm). Maximum projections of hCD63-GFP and 6E10 were converted to binary and run through ImageJ's Colocalization plugin to generate GFP/6E10 colocalized pixels. (**C**) Comparison of hCD63-GFP puncta colocalized with 6E10 staining in 6E10^{+}MET^{+} and 6E10^{+}MET^{-} plaques in the cortex of 13mo. male (n = 3 mice/group) and female (n = 3 mice/group) APP$^{NL\text{-}F/NL\text{-}F}$ CD63$^{f/+}$ mice. 3D projections of individual plaques were created from the 6E10 channel in Imaris and used to delineate plaque-associated hCD63-GFP signal. Puncta counts were normalized to plaque volume and compared. *P* values determined by Student's *t*-test and data shown as mean ± SEM. (**D**) Representative electron micrograph (2500× magnification) of mature fibrillar Aβ plaque in the somatosensory cortex of APP$^{NL\text{-}F/NL\text{-}F}$CD63$^{f/+}$ mice (23mo.) following AAV8-CaMKII-mCherry-Cre injections (plaque core at green asterisk;

scale bar = 2 μm). Boxes indicate the approximate locations of **E** (red box) and **F** (yellow box). High-magnification electron micrographs of 5 nm immunogold-labelled GFP from neuron-derived hCD63-GFP were found to be primarily localized in and around peripheral amyloid fibrils (**E**; black arrowheads; 30,000× magnification, scale bar = 100 nm) but were absent within the dense fibrillar core (**F**; 20,000× magnification, scale bar = 200 nm).

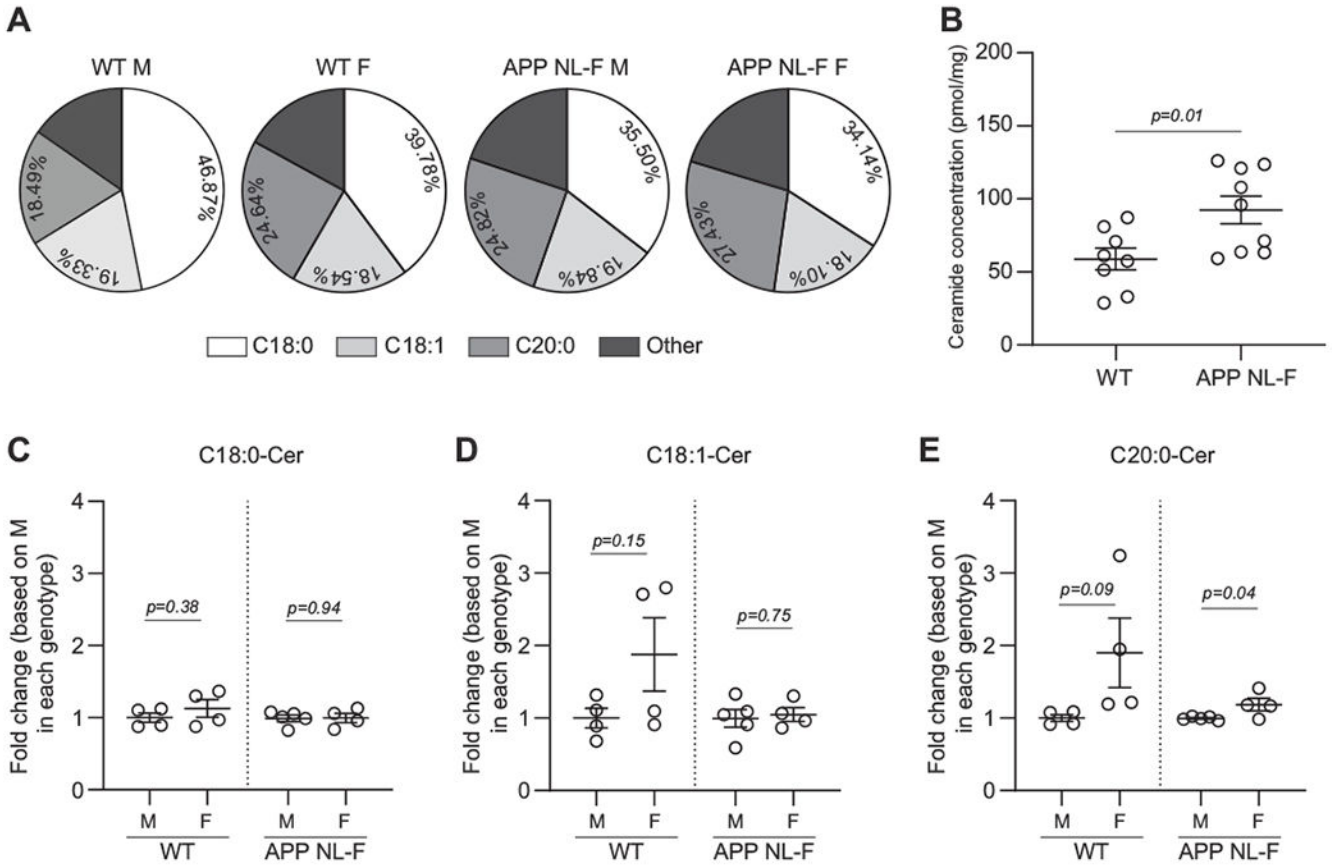

Fig. 3.

HPLC-MS/MS analysis of somatosensory cortex ceramide species from WT and APP NL-F mice.

(A) Composition of major ceramide species (*i.e.*, close to or >20% of total ceramide) in cortical samples from 14 to 15-month-old male and female WT and APP NL-F mice. (**B**) Total ceramide levels normalized to sample protein concentration (pmol/mg) in tissue samples from WT and APP NL-F mice. Fold-change relative to respective males of C18:0-Cer (**C**), C18:1-Cer (**D**), and C20:0-Cer (**E**) in WT and APP NL-F groups. Absolute levels of C18:0-Cer, C18:1-Cer, and C20:0-Cer were normalized to protein concentration. To reduce batch-related variability, relative values based on males from each batch were calculated and compared to determine the sex differences. *P* values determined by Student's by *t*-test and data shown as mean ± SEM; $n = 4–5$ mice/group.

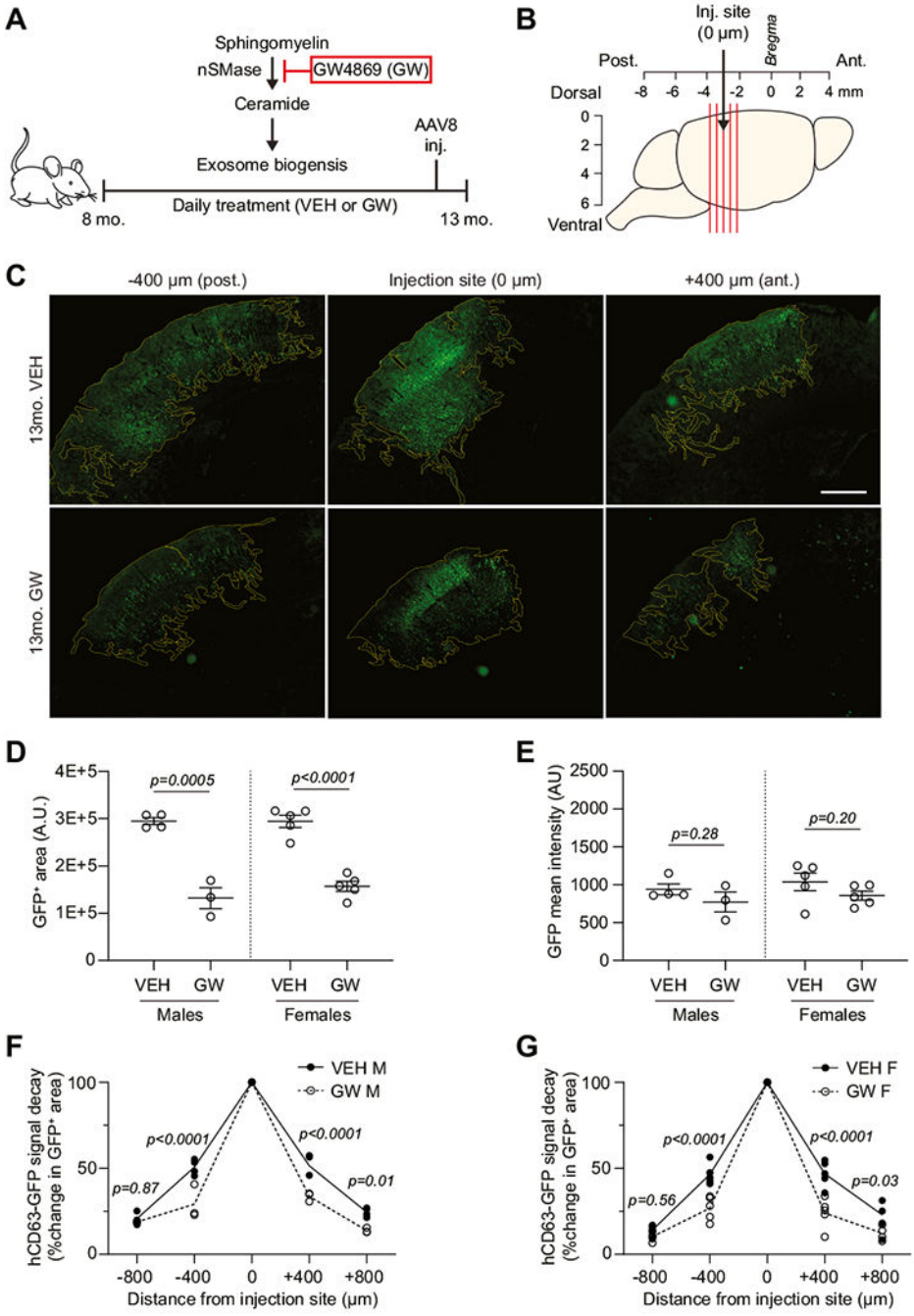

Fig. 4.

GW4869 effectively suppresses spreading of neuron-derived exosomes in male and female APP NL-F mice *in vivo*.

(**A**) Schematic diagram of GW4869 treatment paradigm at early disease stages from 8mo to 13mo. 8-month-old male and female $APP^{NL\text{-}F/NL\text{-}F}CD63^{f/+}$ mice were randomly assigned to receive daily treatment with vehicle (VEH) or GW4869 (GW). A focal injection of AAV8-CaMKII-mCherry-Cre to induce expression of neuron-specific hCD63-GFP was performed in the lateral isocortex (−3.00 mm A/P, +3.50 mm M/L, −0.9 mm D/V) of a subset of mice

two weeks prior to the end of treatments (13mo). (**B**) Schematic representation of cortical injection site (black arrow) and approximate locations of coronal sections examined for exosome spreading (red lines) along the anterior (Ant.)-posterior (Post.) axis in the cortex. (**C**) Representative images of hCD63-GFP signals ±400 μm relative to the injection site (0 μm) in 13-month-old VEH- and GW-administered APP NL-F mice; 2.5×-magnification; scale = 500 μm. Quantification of hCD63-GFP$^+$ area (A.U.; **D**) and mean signal density (A.U.; **E**) at the injection site in VEH and GW males and females; *p* values determined by Student's *t*-tests and data shown as mean ± SEM. Quantification of hCD63-GFP$^+$ signal decay on sections anterior/posterior to the injection site in VEH and GW males (**F**) and females (**G**), calculated as the percentage of hCD63-GFP$^+$ area at each distance relative to hCD63-GFP$^+$ area at the injection site (set as 100% for each mouse). All quantifications of hCD63-GFP$^+$ area is restricted in the cortex. P values determined by Two-way ANOVA for males (interaction: F (Ferretti et al., 2018; Tabatadze et al., 2010)=7.348, $p = 0.0006$; distance: F (Ferretti et al., 2018; Tabatadze et al., 2010)=364.8, $p < 0.0001$; treatment group: F (Ferretti et al., 2018; Tabatadze et al., 2010)=43.35, $p < 0.0001$; F) and females (interaction: F (Ferretti et al., 2018; Puglielli et al., 2003)=6.560, $p = 0.0004$; distance: F (Ferretti et al., 2018; Puglielli et al., 2003)=329.7, $p < 0.0001$; treatment group: F (Ferretti et al., 2018; Puglielli et al., 2003)=42.95, $p < 0.0001$; G) and data shown as mean ± SEM; n = 4 VEH M, 3 GW M, 5 VEH F, and 5 GW F.

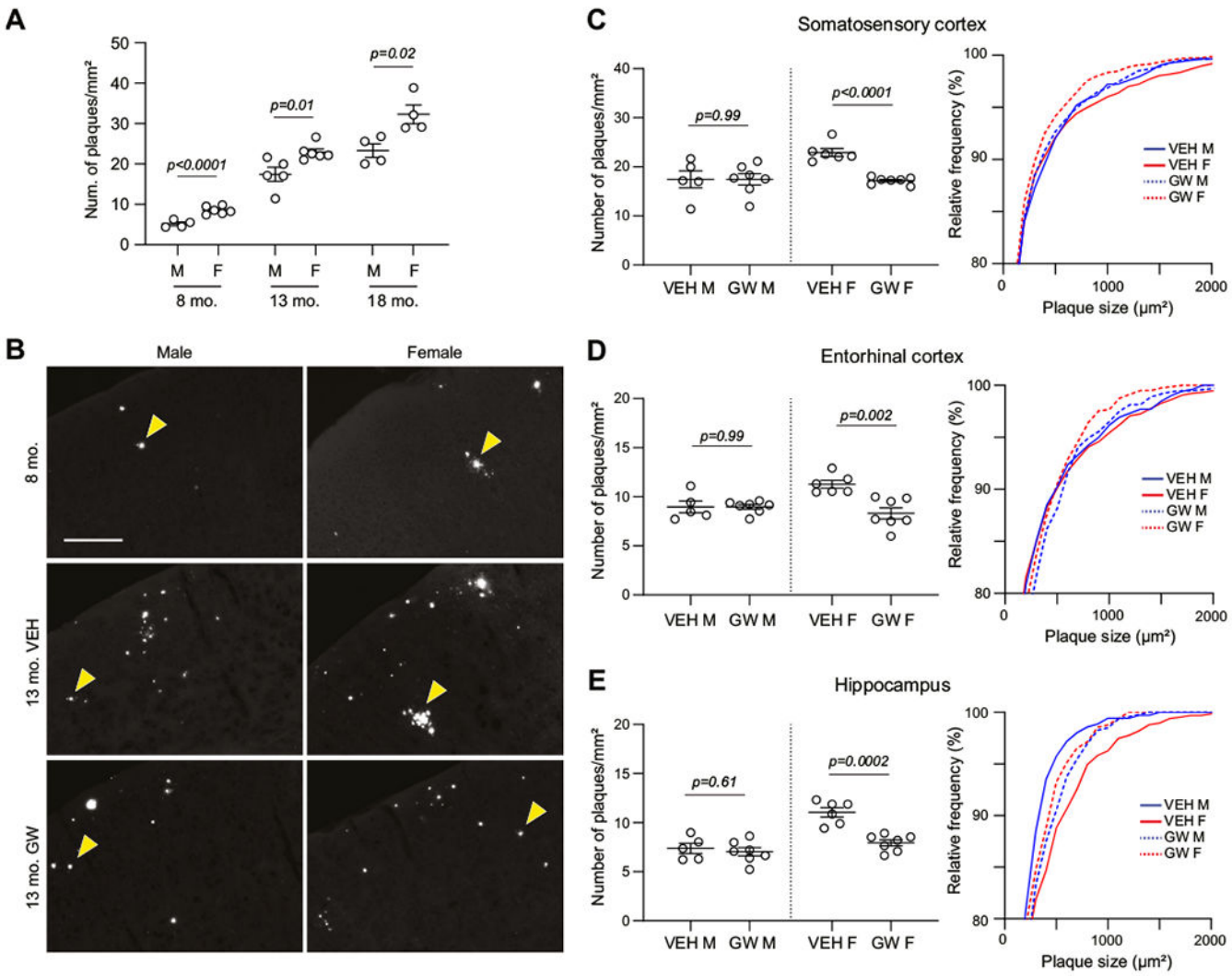

Fig. 5.

Chronic inhibition of nSMase during the early disease stage selectively attenuates amyloid pathology in female but not male APP NL-F mice.

(**A**) Comparison of Aβ plaque numbers in somatosensory cortex of male and female APP NL-F mice at 8, 13, and 18mo. The number of individual methoxy-X04 (MET)-labelled plaques per image (10× magnification) was normalized to plaques/mm^2 and averaged for each mouse; p values determined by Student's t-test and data shown as mean ± SEM; *n* = 8–12 sections/mouse, 4–6 mice/group; (**B**) Representative images (10× magnification) of MET$^+$ Aβ plaques (white arrows) in the somatosensory cortex of 8mo. untreated APP NL-F mice, 13mo. VEH, and GW APP NL-F mice; scale = 200 µm. Quantification of MET$^+$ Aβ plaques from the somatosensory cortex (**C**), entorhinal cortex (**D**), and hippocampus (**E**) of 13mo. VEH. and GW treated APP NL-F mice. The quantification was performed per image within each region and normalized to mm^2; data shown as mean ± SEM; plaque size distribution curves were calculated from individual plaques sizes (µm^2). Only partial plaque size distribution (> 80% frequency) was shown. The full-size distribution frequency was shown in Supplemental Fig. 5. n = 8–12 sections/mouse, 5–7 mice/group.

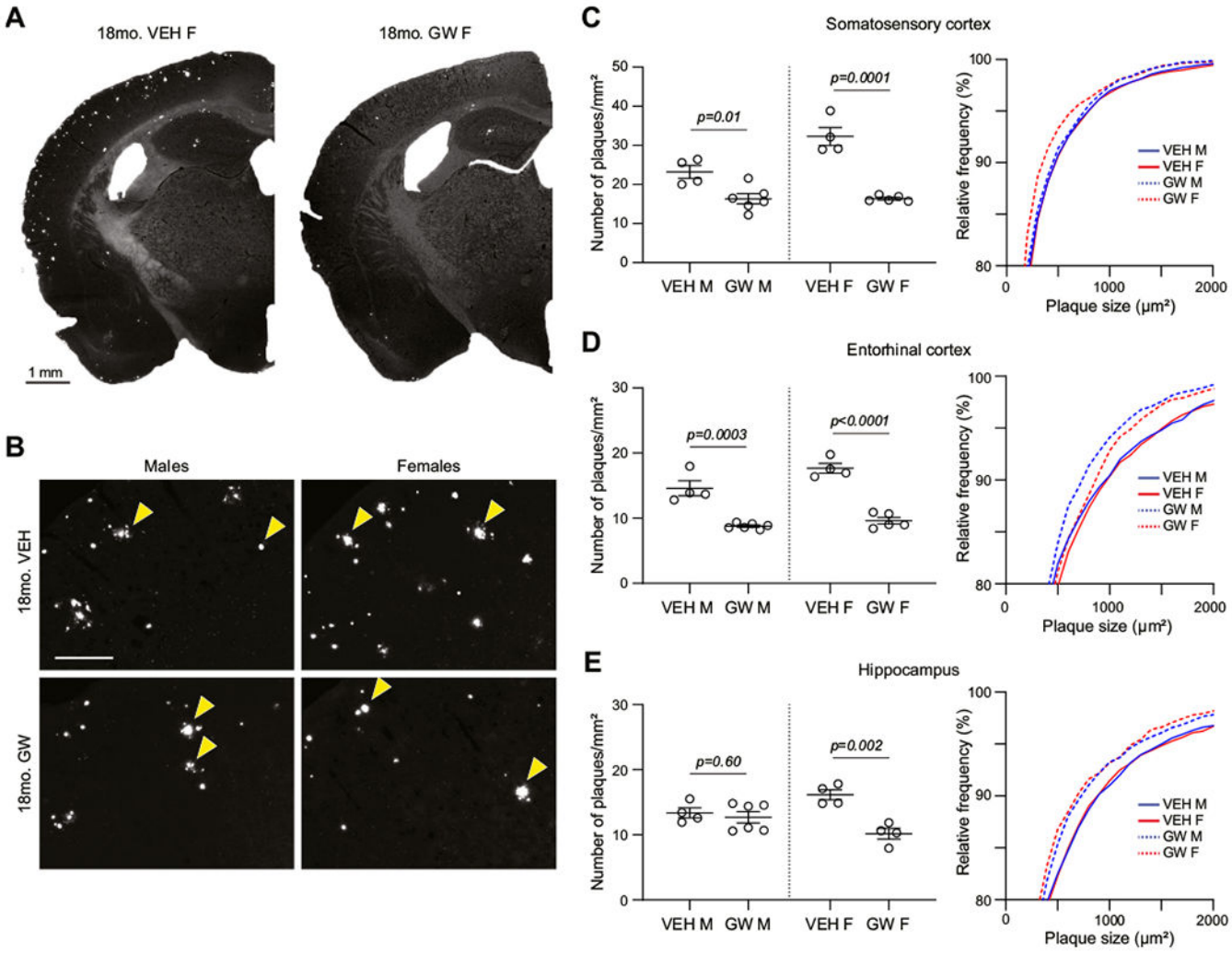

Fig. 6.

Chronic inhibition of nSMase at the disease progression stage preferentially attenuates amyloid pathology in female APP NL-F mice.

(**A**) Representative brain images of overall MET$^+$ Aβ plaques in mid-brain coronal sections from 18mo. VEH and GW APP NL-F female mice; 2.5× magnification stitched images; scale bar = 1 mm. (**B**) Representative images of MET+ Aβ plaques (yellow arrows) in the somatosensory cortex of 18mo. VEH and GW APP NL-F male and female mice; 10× magnification; scale bar = 200 µm. Quantification of MET$^+$ Aβ plaques from in the somatosensory cortex (**C**), entorhinal cortex (**D**), and hippocampus (**E**) of 18mo. VEH. and GW treatment APP NL-F mice. The quantification was performed per image within each region and normalized to mm^2; data shown as mean ± SEM; plaque size distribution curves were calculated from individual plaques sizes (µm^2). Only partial plaque size distribution (> 80% frequency) was shown. The full-size distribution frequency was shown in Supplemental Fig. 5. n = 14–16 sections/mouse, 4–6 mice/group.

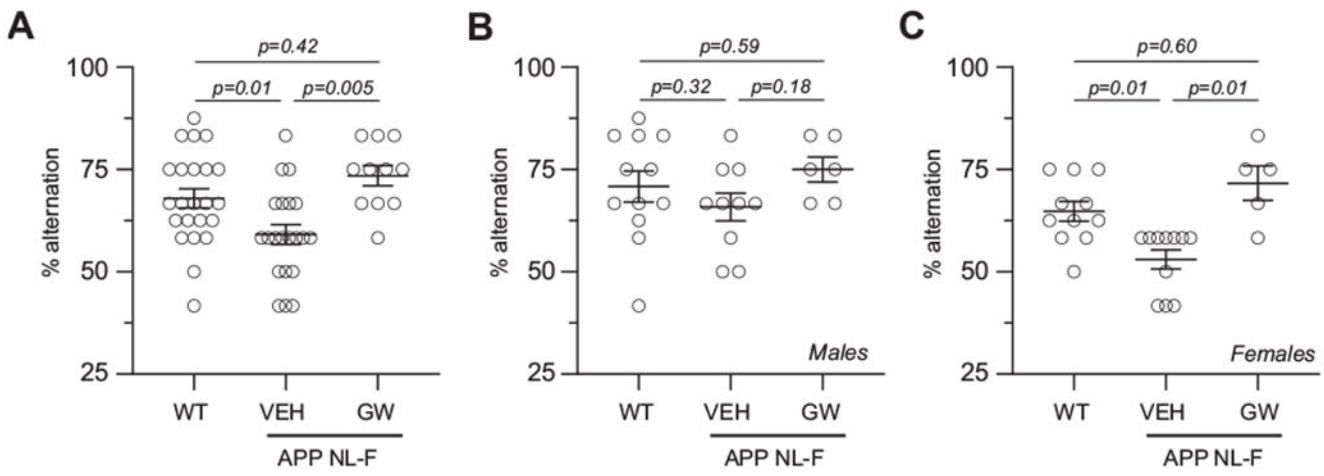

Fig. 7.

All data sets supporting this current study are available upon request to the corresponding author.alternation behavior (SAB) of mice from age-matched WT, VEH- (VEH-treated + untreated APP NL-F mice) and GW treatment APP NL-F mice (18mo) after T maze trials. SAB was calculated as the percent alternation across a total of 12 T maze trials, $n = 24$ WT, 21 VEH APP NL-F, and 11 GW APP NL-F mice. No differences were observed between VEH-treated and untreated APP NL-F mice. SAB comparison among male groups (**B**; $n =$ 12 WT, 10 APP NL-F, and 6 GW APP NL-F mice) and female groups (**C**; n = 12 WT, 11 APP NL-F, and 5 GW APP NL-F mice). *P* values determined by one-way ANOVA with Tukey post-hoc test (A: F(2, 52) = 7.424, $p = 0.0015$; B: F (Serrano-Pozo et al., 2011; Dinkins et al., 2016)=1.287, $p = 0.2937$; C: F (Serrano-Pozo et al., 2011; Dinkins et al., 2014)=10.72, $p = 0.0005$) and data shown as mean ± SEM.